Excited State Spectroscopy of Boron Vacancy Defects in Hexagonal Boron Nitride using Time-Resolved Optically Detected Magnetic Resonance

Simon Baber,[†] Ralph Nicholas Edward Malein,[†] Prince Khatri,[†] Paul Steven Keatley,[†] Shi Guo,[†] Freddie Withers,[†] Andrew J. Ramsay,[‡] and Isaac J. Luxmoore[*,†]

†*College of Engineering, Mathematics and Physical Sciences, University of Exeter, Exeter, EX4 4QF, United Kingdom.*

‡*Hitachi Cambridge Laboratory, Hitachi Europe Limited, Cambridge, CB3 0HE, United Kingdom*

E-mail: i.j.luxmoore@exeter.ac.uk

Abstract

We report optically detected magnetic resonance (ODMR) measurements of an ensemble of spin-1 negatively charged boron vacancies in hexagonal boron nitride. The photoluminescence decay rates are spin-dependent, with inter-system crossing rates of 1.02 ns^{-1} and 2.03 ns^{-1} for the $m_S = 0$ and $m_S = \pm 1$ states, respectively. Time-gating the photoluminescence enhances the ODMR contrast by discriminating between different decay rates. This is particularly effective for detecting the spin of the optically excited state, where a zero-field splitting of $|D_{ES}| = 2.09$ GHz is measured. The magnetic

field dependence of the photoluminescence exhibits dips corresponding to the Ground (GSLAC) and excited-state (ESLAC) anti-crossings and additional anti-crossings due to coupling with nearby spin-1/2 parasitic impurities. Comparison to a model suggests that the anti-crossings are mediated by the interaction with nuclear spins, and allow an estimate of the ratio of the singlet to triplet spin-dependent relaxation rates of $\kappa_0/\kappa_1 = 0.34$.

Keywords

Color center, hexagonal boron-nitride, 2D materials, optically detected magnetic resonance

Hexagonal boron nitride (hBN) is a van der Waals crystal with a wide band gap, and is often used as an insulator in layered two-dimensional devices. Recently, color centers in hBN have attracted considerable attention as room temperature quantum emitters.[1] Not only can high brightness anti-bunching be observed at room temperature,[2,3] but for some defect species, the zero phonon line fraction can be as high as 80%,[1,4] and can exhibit transform-limited linewidths under resonant excitation at room temperature.[5,6] These results suggest promising optical coherence properties that surpass defects found in other wide band gap materials such as diamond[7] or silicon carbide.[8] More recently, optically detected magnetic resonance (ODMR) experiments have also been reported.[9–18]

So far, ODMR experiments using hBN have mainly focused on ensembles of negatively charged boron vacancies (V_B^-),[9–15] although there have also been reports of experiments with single bright defects of unconfirmed species.[17,18] The optical properties of (V_B^-) are not as impressive as other defects in hBN, with phonon-broadened emission and low quantum yield.[19] However, work to date has revealed promising spin properties with V_B^- a radiative spin triplet system (total spin quantum number, $S = 1$), with a zero-field splitting of $D_{GS} = +3.45$ GHz.[9] So far, the focus has been on the spin properties of the optical ground-state (GS), and nothing is known experimentally about the spin-properties of the excited state

(ES), which plays an important role in the spin read-out and pumping process. Furthermore, knowledge of the spin-splittings of the ES may provide further confirmation of the identity of the defect currently assigned to V_B^-.

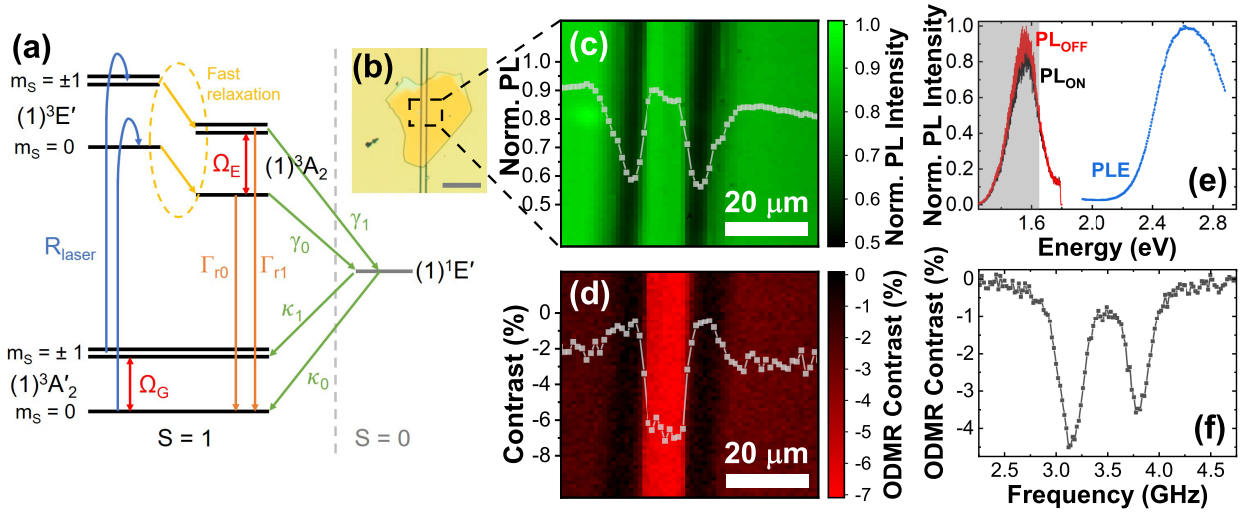

Figure 1: (a) Energy level diagram of the V_B^- defect in hBN (adapted with permission from Ref. 19. Copyrighted by the American Physical Society). (b) Optical micrograph of the coplanar waveguide device with hBN flake on top. The scale marker is 100 μm (c) Spatial map of the photoluminescence (spectral range from 1.2 to 1.65 eV) from the region indicated by the dashed square in (b). (d) Spatial map of the ODMR contrast for the ground state $m_S = 0 \leftrightarrow -1$ transition at a magnetic field of 12 mT, from the same region as in (c). Intensity and contrast profiles along the x-direction, taken from the centre of the images, are overlaid in (c) and (d), respectively. (e) PL and PLE spectra of the V_B^-. The gray shaded area indicates the spectral band over which the PL signal is integrated. PL spectra are plotted with and without the microwave excitation. (f) ODMR spectrum of the V_B^- ensemble with a magnetic field of 12 mT.

In this work, we present ODMR experiments with an ensemble of negatively charged boron vacancies in hBN flakes transferred directly onto microfabricated co-planar waveguides (CPW). The close proximity of the hBN flake to the CPW results in a large ac-magnetic field at the defects. In combination with a time gated detection method, which enhances the ODMR contrast to $\sim 30\%$, we are able to observe resonances corresponding to the spin-levels of the optical ES. In Fig. 1(a) an energy level diagram based on the theoretical work of Reimers *et al.*[19] is presented. In this picture, the optical cycle in the triplet subspace consists of absorption from the GS, $(1)^3A_2'$, which is dominated by the transition to $(1)^3E'$, followed by

fast (sub-ps) relaxation to $(1)^3A_2$ and radiative recombination back to $(1)^3A_2'$. We measure a zero-field splitting (ZFS) of $|D_{ES}| = 2.1$ GHz for the ES spin levels and a g-factor that is similar to the GS value of $\sim$2. The PL decay rates are found to be spin-dependent, and measured to be $\gamma_0 = 1.01$ ns^{-1}, and $\gamma_1 = 2.03$ ns^{-1}. This is fast compared with the estimated radiative rate and consistent with estimates of inter-system-crossing (ISC) times calculated in ref.[19] This spin-dependent relaxation gives rise to the spin read-out contrast. To cross-check the ODMR measurements, the magnetic field dependence of the PL is measured. Dips occur at the expected anti-crossings in the ground and excited states in a microwave-free analog of ODMR. In addition, there are dips that indicate the presence of nearby spin-1/2 defects, that may provide a source of decoherence.

Fig. 1(b) shows an image of our device, consisting of a gold coplanar waveguide (CPW) fabricated on a sapphire substrate. HBN flakes are obtained by mechanical exfoliation from bulk crystal and positioned on the CPW using standard dry-transfer techniques. Boron vacancies are introduced/activated using Carbon-ion implantation at 10 keV and a dose of 1×10^{14} cm^{-2}.[14] Photoluminescence (PL) is excited using a broadband supercontinuum laser filtered by an acousto-optic tunable filter (AOTF) to give a $\sim$1 nm bandwidth and a pulsewidth of $\sim$5 ps. All experiments are performed at room temperature and in air (further details can be found in the Supporting Information [S.I.]).

The PL spectrum from the implanted flake is shown in Fig. 1(e), with a broad emission peak centred at around 1.56 eV, consistent with previous measurements.[9] The emission is uniform across the flake, and enhanced where the flake overlaps the metal of the CPW, as shown by the PL intensity map in Fig. 1(c). The excitation efficiency depends on the energy of the laser, with a PLE spectrum presented in Fig. 1(e). The absorption peaks at around 2.6 eV, close to the energy of the $(1)^3A_2' \rightarrow (1)^3E'$ transition, predicted by Reimers *et al.*[19] to dominate the absorption. In the following experiments the laser is tuned to 2.6 eV to match the peak of this absorption.

In the case of continuous wave (CW) ODMR, a microwave signal is modulated on and

off, and the contrast (defined as $(I_{on} - I_{off})/I_{off}$ where I_{on} and I_{off} are the PL intensity with the microwaves on and off, respectively) is measured. A typical CW-ODMR spectrum is plotted in Fig. 1(f) for a magnetic field of 12 mT. The two resonances at ~ 3.1 GHz and ~ 3.8 GHz correspond to the $m_S = 0$ to $m_S = -1$ and $m_S = 0$ to $m_S = +1$ transitions in the optical GS.[9] The ODMR contrast of the $m_S = 0$ to $m_S = -1$ transition is mapped across the sample in Fig. 1(d), with strong contrast only observed from the central conductor of the CPW, where the ac-magnetic field has a strong in-plane component.

In previous work with NV-centers in diamond[20] and divacancies in SiC,[21] the spin-dependent lifetimes of the time-resolved photoluminescence (TRPL) was used as a contrasting agent. We now trial this method for the V_B^- in hBN. In Fig. 2(a) the pulse-sequence is illustrated. To optically excite the sample, the 39 MHz pulse train is modulated at a repetition frequency of 100 kHz and a duty-cycle of 95 %. The 9.5μs train of pulses optically pump the ensemble of boron vacancies into the ground $m_S = 0$ state.[9] To rotate the spin of the GS, synchronized microwave pulses are applied at 50 kHz, half the optical repetition frequency. Fig. 2(b) shows the photoluminescence signal versus arrival time relative to the microwave pulses, ΔT. This is averaged over many repetition periods of the laser, which is not time synchronised with the microwave pulses. This results in the PL trace shown in Fig. 2(b), which is equivalent to that recorded with a CW laser. Following a microwave pi-pulse the signal drops, then recovers as the laser optically pumps the system back into the $m_S = 0$ state.

TRPL traces are made from the same data set, by time-binning the photon arrival times, δt relative to the 39 MHz repetition rate of the laser. The PL is averaged over the ~ 39 pulses that lie within the 1 μs long windows highlighted in Fig. 2(b). Such TRPL traces are plotted in Fig. 2(c) with and without a microwave pi-pulse. Applying the microwave pulse reduces the overall intensity, and speeds up the PL decay. The TRPL curves of Fig. 2(c) are fit with a bi-exponential decay of the form $A_0 e^{-t\gamma_0} + A_1 e^{-t\gamma_1}$ (convolved with a Gaussian of 330 ps FWHM to account for the detector response), yielding PL decay rates $\gamma_0 = 1.01$ ns^{-1}

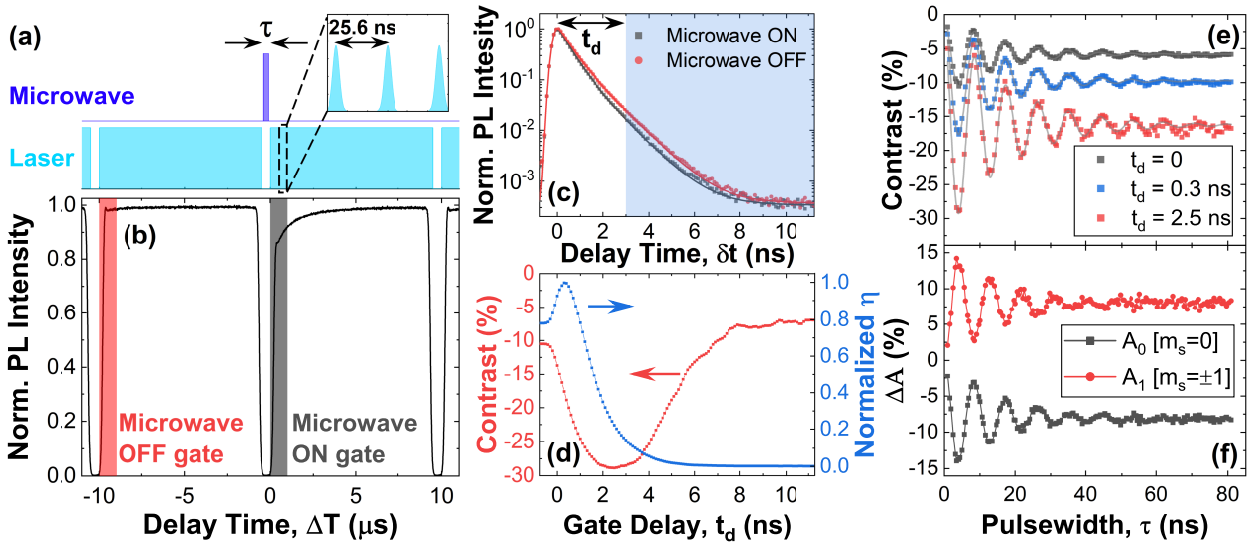

Figure 2: Enhanced contrast of ODMR using time filter. (a) Pulse sequence for time-resolved ODMR measurements. (b) Typical time-averaged PL intensity trace resulting from pulse sequence in (a), for time-binning of photons by their arrival time relative to the microwave pulse, ΔT. The red and gray shaded regions indicate the collection windows used to plot time-resolved photoluminescence traces. (c) Time-resolved PL traces for time-binning of photons by their arrival time relative to the laser pulses, δt. The black and red cures are for photons detected during the microwave on and off windows shown in (b), respectively. The PL counts for both traces are normalized to the maximum value of the microwave OFF trace. The gate delay time, t_d, is defined from the peak of the time-resolved PL trace, with the blue shaded region indicating the photons which are used to calculate the contrast plotted in (d). (d) Time-resolved contrast and sensitivity figure of merit, η for a microwave pi-pulse. (e) ODMR contrast as a function of microwave pulsewidth, τ, showing Rabi-oscillation of the $m_S = 0$ to $m_S = -1$ ground state transition. At each pulsewidth time-resolved traces are recorded and the contrast is calculated for the three different gate delay times indicated. (f) From the same data set as (e) exponential amplitudes are extracted from bi-exponential fits to the time-resolved PL curves and the change in these coefficients between when the microwave pulse is on and off, $\Delta A_{0,1} = \left(A_{0,1(on)} - A_{0,1(off)}\right) / \left(A_{0(off)} + A_{1(off)}\right)$, is plotted. In all panels the external magnetic field is 12 mT.

and $\gamma_1 = 2.03$ ns^{-1}. Applying a microwave pi-pulse, enhances the fast (A_1), and suppresses the slow (A_0) component of the PL decay. If optical pumping initializes the GS into $m_S = 0$ state,[9] this implies that the fast decay can be assigned to $m_S = \pm 1$, and the slow decay to $m_S = 0$ of the ES. In ref. 19, the relaxation of the optical ES, $(1)^3A_2$, was predicted to be dominated by ISC to $(1)^1E'$. The ISC-lifetime was calculated to be 1.7 ns at room temperature, compared to a radiative lifetime of 11 μs, in reasonable agreement with our measurements. This spin-dependence of the ISC rates gives rise to the ODMR contrast.

Since the PL decay rates are spin dependent, the ODMR contrast can be enhanced by selecting only the photons that arrive after a gate-time, t_d, with respect to the laser pulse. In Fig. 2(d), the contrast, $C(t) = [I_{ON}(t) - I_{OFF}(t)]\,/I_{OFF}(t)$ is plotted vs t_d, where I_{ON} and I_{OFF} are the integrated counts from t_d to $t_{rep}/2$ for the microwave ON and OFF traces, respectively, and t_{rep} is the repetition period of the laser. At $t_d = 0$, the full signal is collected and the contrast for a microwave π-pulse is $\sim$ 10%. The contrast increases with t_d, reaching an optimum of almost 30% at $t_d \approx 2.5$ ns, a $\sim$ 3-fold enhancement. To quantify the improvement in sensitivity of the time-gated readout, we calculate a figure of merit, $\eta(t) = (I_{ON}(t) + I_{OFF}(t))\,C(t)^2$, which is plotted as a function of t_d in Fig. 2(d). This is proportional to the sensitivity of an ODMR B-field sensor,[22] and shows a modest improvement of $\sim$ 20% at $t_d = 0.3$ ns. To illustrate the enhancement in contrast due to time-gating, Fig. 2(e) compares Rabi-oscillation measurements with a gate delay of $t_d = 0$ (no time-gating), $t_d = 0.3$ ns (maximum η) and $t_d = 2.9$ ns (maximum contrast). A Rabi oscillation measurement can also be made by plotting the relative change in the amplitudes of the exponential components A_0, and A_1 vs microwave pulse width, τ (Fig. 2(f)). Note that the change in amplitude is equal and opposite ($\Delta A_0 \approx -\Delta A_1$), indicating the transfer of population from $m_S = 0 \leftrightarrow -1$, and confirming that the read-out contrast arises from the spin-dependent decay rates.

The close proximity of the hBN flake to the CPW enables a strong ac-magnetic field, and a Rabi-frequency reaching $\sim$ 110 MHz, limited by the maximum available input power

of +30 dBm (see S.I.). The combination of strong ac-field and time-gating allows detection of the spin structure of the ES, despite the fast ISC times. Figure 3(a) presents a PL time-trace, with the pump laser always on. Following resonant microwave excitation of the GS $m_S = 0 \leftrightarrow -1$ transition, there is a rapid drop in PL signal, which recovers when the microwaves are switched off, indicating the microwave excitation is strong enough to overcome the optical pumping. Figure 3(b) compares ODMR spectra taken with the laser on/off during microwave excitation, using the time-gated method, at a B-field of 12 mT. When the laser is off, only two Zeeman-split peaks centered on the ZFS $|D_{GS}| \approx 3.5$ GHz, matching the GS are observed.[9] However, if the laser is on during microwave excitation, an excited state doublet with ZFS $D_{ES} \approx 2.1$ GHz is also observed. Fig. 3(e,f) present a color-map of the ODMR spectra vs B-field. A third, much weaker, transition with ZFS of ~ 7.5 GHz is also observed.

Interestingly, the contrast vs gate-time reveals different behavior for the ES and GS transitions[23] (see also S.I.). In Fig. 3(c), the contrast is plotted versus gate-time for excitation frequencies corresponding to the GS ($m_S = 0$ to $m_S = -1$ [3.14 GHz]) and ES ($m_S = 0$ to $m_S = +1$ [2.44 GHz]) transitions with a magnetic field of 12 mT. Without time gating the GS contrast is -7.1 % and decreases rapidly with t_d, reaching a maximum negative contrast of -20% at $t_d = 1.7$ ns. An increase of 2.8 times, similar to the case of pulsed ODMR, in the laser off case, shown in Fig. 2. For the ES, the contrast without time gating is -2.1% and the initial rate of decrease is slower than for the GS, but the rate then increases and reaches a maximum contrast of -16% at $t_d = 3.4$ ns, an enhancement of 7.5 times. As shown in Fig. 3(d) this translates to different gate delay times for optimum read-out sensitivity of the GS and ES. For the GS (ES) the read-out sensitivity is increased by 1.5 times at $t_d = 0.5$ ns (3 times at $t_d = 3.4$ ns). The time gated detection therefore plays a crucial role in resolving the ES transitions, as highlighted in the S.I and hence the data in Fig. 3(f) is plotted for $t_d = 3.4$ ns.

The resonant frequencies of the GS and ES transitions versus magnetic field are plotted

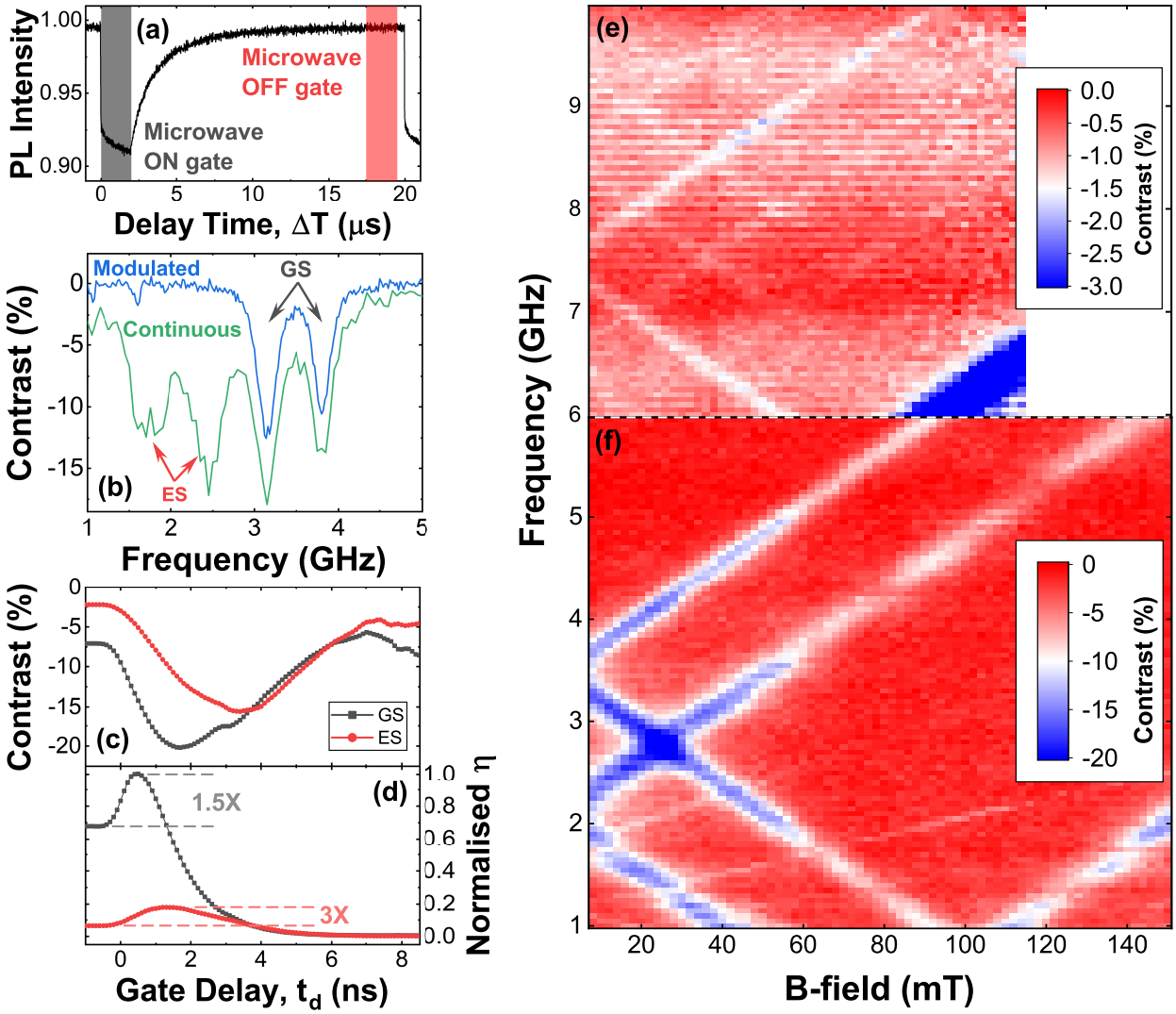

Figure 3: Zeeman splitting of ground and excited states of the negatively charged boron vacancy. (a) Time averaged PL intensity resulting from a $2\mu s$ microwave pulse with a repetition rate of 50 kHz. (b) Comparison of ODMR spectra for microwave excitation applied with and without the laser applied. (c) and (d) Time resolved contrast (c) and sensitivity figure of merit, η (d) for microwave excitation of the ground ($m_S = 0$ to $m_S = -1$ [3.14 GHz]) and excited ($m_S = 0$ to $m_S = +1$ [2.44 GHz]) states. The curves in (d) are normalized to the maximum of η for the ground state transition. (e) and (f) Color plots of the ODMR contrast as a function of microwave frequency and external magnetic field for $t_d = 3.4$ ns. In (e) the contrast scale is limited to -3 % to highlight the transition with ~ 7.5 GHz ZFS. In (a) - (d) the external magnetic field is 12 mT.

in Fig. 4(a), and fitted to:

$$\nu_{-,+} = \frac{1}{h}\left(D \pm \sqrt{E^2 + (g\mu_B B)^2}\right) \tag{1}$$

where D and E are the ZFS parameters, μ_B is the Bohr-magneton and g the electron g-factor.[9] We find values of $D_{GS}/h = 3.47$ GHz, $E_{GS}/h = 126$ MHz and $g_{GS} = 2.001$ for the GS, in broad agreement with previous reports,[9–15] and $|D_{ES}/h| = 2.09$ GHz, $|E_{ES}/h| = 154$ MHz and $g_{ES} = 1.980$ for the ES. The ES resonances are broad, and independent of the external magnetic field, with a full-width half maximum (FWHM) of ~ 400 MHz. This is roughly consistent with the FWHM expected from the ES lifetime, $FWHM = (\gamma_0 + \gamma_{\pm 1})/\pi = 0.97$ GHz.[24]

Our results are consistent with the theoretical work of Reimers *et al.*[19] We assign the ES with ZFS of 2.09 GHz to the $(1)^3A_2$ level. The origin of the transition with ZFS of 7.5 GHz is uncertain. It could originate from another, unidentified defect species within our sample, but it seems more plausible that it is related to an energy level within the V_B^-. In this case, the most likely candidates would be $(2)^3A_2'$ or $(1)^3A_1''$. However, at room temperature both states are predicted to relax to $(1)^3A_2$ on timescales less than 1 ps, which would account for the weakness of the ODMR contrast, but it seems unlikely that our experiments could resolve a process on this timescale. Further experiments combining temperature dependence, PLE and ODMR could shed further light on the origin of this transition.

Fig. 4(a) also illustrates that anticrossings of the $m_S = 0$ and $m_S = -1$ states are expected at ~ 76 mT and ~ 125 mT, for the excited and ground states, respectively. These anticrossings are investigated by measuring the TRPL as a function of the external magnetic field, with no microwave excitation, see Fig. 4(b). Here, the contrast is defined as $(I_B - I_{ref})/I_{ref}$, where I_B is the PL intensity at the given field and I_{ref} is the reference PL intensity recorded at B=20 mT. Dips in the contrast are observed at 76 mT and 125 mT, as expected for spin mixing at the ESLAC and GSLAC, respectively. In addition, two further minima

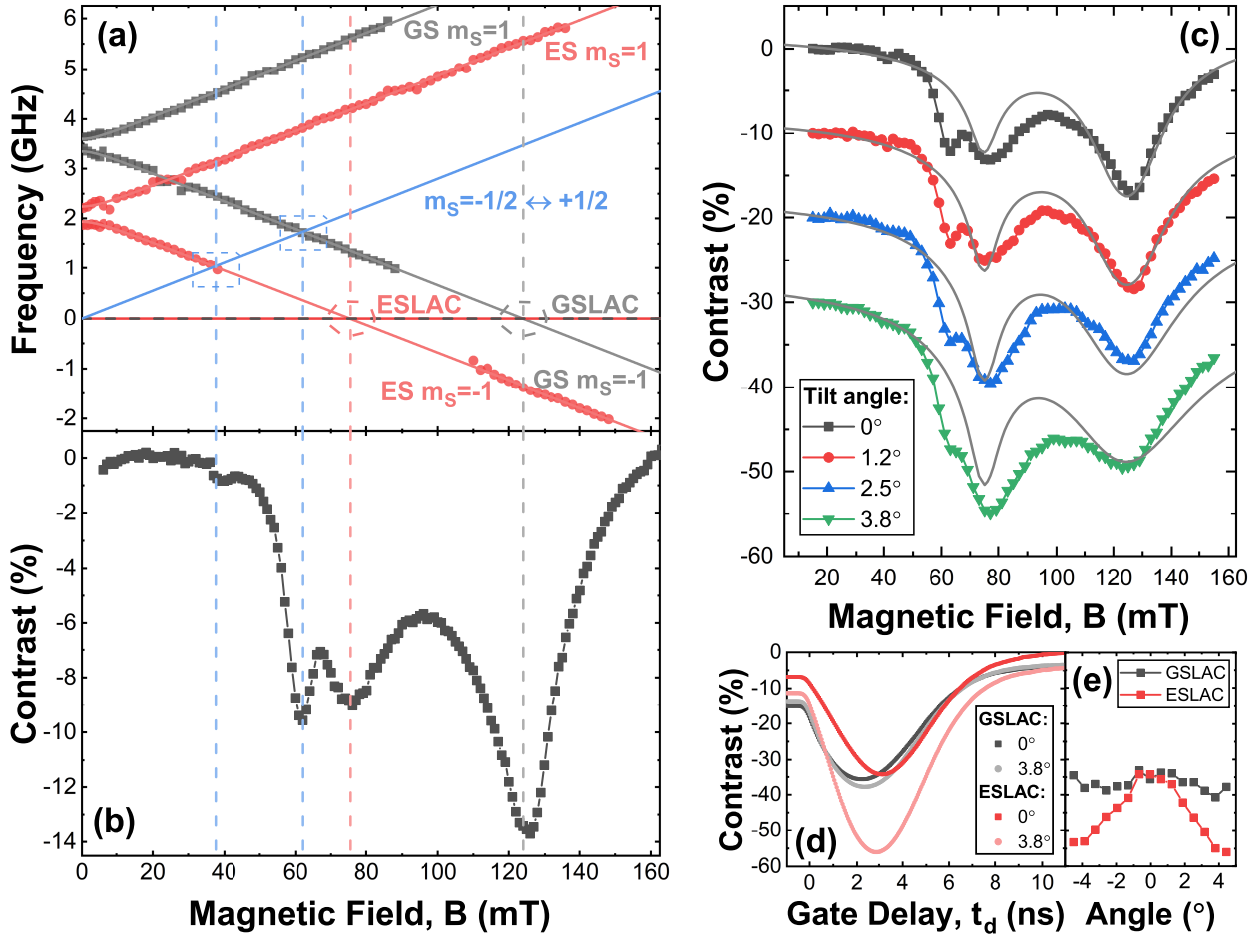

Figure 4: Level anticrossings of the negatively charged boron vacancy. (a) Frequencies of the ground and excited state resonances extracted from Gaussian fits to the data in Fig. 2(d). The solid red (gray) lines show fits to the data of Eq. 1 for the excited (ground) state transitions. The red (gray) vertical dashed lines indicate the magnetic field corresponding to the ESLAC (GSLAC). The solid blue line indicates the frequency difference of a $S = 1/2$ impurity and the dashed blue lines indicate the frequencies at which this anticrosses with the V_B^- ground and excited states. A positive sign of $D_E S$ is assumed. (b) Contrast of the time resolved photoluminescence (defined as $(I_B - I_{ref})/I_{ref}$, where I_B is the PL intensity at the given field and I_{ref} is the reference PL intensity, recorded at 20 mT) as a function of the applied magnetic field. Dips in the intensity at ~ 76 mT and ~ 125 mT correspond to the excited state and ground state level anticrosings, respectively. (c) Magnetic field dependence of the contrast for different tilt angles of the magnetic field relative to the c-axis of the hBN. The curves are offset by -10% for clarity. The solid gray lines show spectra calculated using the model described in the main text and S.I. In (b) and (c) $t_d = 0.5$ ns (d) Time-resolved contrast at the excited and ground state level anticrossings at two tilt angles of the external magnetic field. (e) Plot of the maximum contrast at the ESLAC and GSLAC versus the tilt angle of the magnetic field.

can be seen in Fig. 4(b), a strong feature at $\sim$ 62 mT and a weaker one at $\sim$ 38 mT. As shown in Fig. 4(b), the Zeeman splitting of a spin-1/2 system is resonant with the $m_S = 0 \leftrightarrow -1$ transition in the excited (ground) state of V_B^- at a magnetic field of $\sim$ 38 ($\sim$ 62) mT. Therefore, we propose that these features originate from coupling of the boron vacancies to neighboring paramagnetic defects of another species or charge state, as seen previously for NV centres coupled to nitrogen[25] and P1[26] defects in diamond. The spin dephasing time $T_2^* \approx 19$ ns (extracted from Rabi-oscillation data, see S.I.) and $T_1 = 10$ μs are shorter than previous reports,[10,12,13] which could also indicate high levels of impurities. As our samples are implanted using carbon it is possible these are carbon related. However, PL measurements show no signature of C-related defects[27] and indicate that boron vacancies are the only luminescent defect present in large concentrations. Experiments using samples fabricated with different ion-species[14] and/or laser irradiation,[15] could shed further light on the nature of these defects.

Finally, by tilting the sample with respect to the field axis of the permanent magnet, we investigate the angular dependence of the external magnetic field on spin-level mixing in the excited and ground states. Fig. 4(c) plots the contrast versus magnetic field for different tilt angles. As the angle increases the contrast of the ESLAC increases, whilst the GSLAC dip is relatively unaffected (see also Fig. 4(e)). To understand these microwave-free ODMR spectra a model[28] is studied based on the energy level diagram, and relaxation rates shown in Fig. 1(a). A full description of the model can be found in the S.I. A comparison of the model to data can be found in Fig. 4(c). Since the radiative rate is slow compared with the inter-system-crossing rates, ($\Gamma_R \approx 1/(11\ \mu\text{s}) \ll \gamma_0, \gamma_1$),[19] the read-out contrast is largely determined by the measured values of γ_0, γ_1 and the gate delay time. The dip at $\sim$ 125 mT arises due to the erasure of the spin initialization by the GSLAC. The GSLAC dip is determined by the ratio of the spin-dependent relaxation rates from the singlet back to the triplet, $\frac{\kappa_0}{\kappa_1} \approx 0.34$, and is independent of the absolute value of κ, which we arbitrarily fix as $\kappa_0 = 20\ \mu\text{s}^{-1}$, since in theory it is expected to be slow.[19]

Near the ESLAC, the optically excited spin rotates, erasing the spin read-out and enhancing the contrast in the PL signal. In contrast to the GSLAC dip, the ESLAC dip is determined by the in-plane effective B-field, and the damping of the spin precession. The change in the ESLAC with tilt is large, and can only be explained by an internal in-plane B-field of approximately 140 MHz co-aligned with the external in-plane B-field, and damping that is lifetime-limited by the ISC rates γ_0, γ_1.

The nearest neighbors of a boron vacancy are three nitrogen atoms, with nuclear spin $I(^{14}N) = 1$, and a GS-hyperfine constant of $A_{GS} = 47$ MHz.[11] This suggests a maximum Overhauser field of 141 MHz. In Fig. 4(c), the model curves are calculated assuming the internal B-field is due to the nuclear spins only. For each value of $-3 \leq m_I \leq 3$, a spectra is calculated for an internal $B_z = Am_I$, and $|B_{xy}| = \sqrt{I(I+1) - m_I^2}$. The resulting spectra is calculated as a sum weighted by the degeneracy of the m_I state to yield a spectra of randomly oriented nuclear spins. The overall match to data, where only the ratio $\frac{\kappa_0}{\kappa_1} = 0.34$ is adjustable is good, with the disagreement regarding the width of the ESLAC dip possibly connected to a nuclear pumping effect that is responsible for orienting the in-plane direction of the Overhauser field.

In conclusion, an ODMR study of negative boron vacancies in hBN is reported. The spin dependent inter system relaxation rates responsible for the spin read-out are measured to be $\gamma_0 = 1.01$ ns^{-1} and $\gamma_1 = 2.03$ ns^{-1} for $m_S = 0$ and $m_S = \pm 1$, respectively. Using a time-gated detection scheme to enhance the ODMR contrast, the zero-field splitting of the ES is measured to be $|D_{ES}| = 2.09$ GHz. The magnetic resonances can also be observed in magnetic field dependent PL measurements, from which the ratio of the spin-dependent relaxation rates from the singlet sub-space back into the triplet GS can be estimated. These are key parameters for understanding the spin initialization and read-out behind the ODMR contrast. Questions remain over how the system escapes the singlet sub-space, since Reimers *et al.*[19] predict that κ could be extremely slow, and it is possible that the reset process requires optical excitation. Characterization of the ES spin-structure is also important as

it has potential application in microwave-free sensing[29] and provides a prospective route to optically initialize the nuclear spins via optical pumping at the ESLAC.[21,30–33] This could lead to improved electron coherence times and is an important challenge for this system, if it is to be used as a resource in quantum control and sensing experiments and applications.[21]

Note: during the review of this manuscript, we became aware of related works studying the spin properties of the V_B^- excited state.[34,35]

Acknowledgement

This work was supported by the Engineering and Physical Sciences Research Council [Grant numbers EP/S001557/1, EP/026656/1, EP/L015331/1 and EP/R008809/1]. Ion implantation was performed by Keith Heasman and Julian Fletcher at the University of Surrey Ion Beam Centre. We thank W. L. Barnes for useful discussions and support.

Supporting Information Available

Further experimental details, power dependent Rabi-oscillation measurements, ODMR contrast plots for different gate delay times, detailed description of Quantum Toolkit in Python[36,37] [QuTIP] and rate equation models.

References

(1) Sajid, A.; Ford, M. J.; Reimers, J. R. Single-photon emitters in hexagonal boron nitride: a review of progress. **2020**, *83*, 044501.

(2) Tran, T. T.; Bray, K.; Ford, M. J.; Toth, M.; Aharonovich, I. Quantum emission from hexagonal boron nitride monolayers. *Nature Nanotechnology* **2015**, *11*, 37–42.

(3) Jungwirth, N. R.; Calderon, B.; Ji, Y.; Spencer, M. G.; Flatté, M. E.; Fuchs, G. D.

Temperature Dependence of Wavelength Selectable Zero-Phonon Emission from Single Defects in Hexagonal Boron Nitride. *Nano Letters* **2016**, *16*, 6052–6057.

(4) Tran, T. T.; Elbadawi, C.; Totonjian, D.; Lobo, C. J.; Grosso, G.; Moon, H.; Englund, D. R.; Ford, M. J.; Aharonovich, I.; Toth, M. Robust Multicolor Single Photon Emission from Point Defects in Hexagonal Boron Nitride. *ACS Nano* **2016**, *10*, 7331–7338.

(5) Hoese, M.; Reddy, P.; Dietrich, A.; Koch, M. K.; Fehler, K. G.; Doherty, M. W.; Kubanek, A. Mechanical decoupling of quantum emitters in hexagonal boron nitride from low-energy phonon modes. *Science Advances* **2020**, *6*, eaba6038.

(6) Dietrich, A.; Doherty, M. W.; Aharonovich, I.; Kubanek, A. Solid-state single photon source with Fourier transform limited lines at room temperature. *Phys. Rev. B* **2020**, *101*, 081401.

(7) Awschalom, D. D.; Hanson, R.; Wrachtrup, J.; Zhou, B. B. Quantum technologies with optically interfaced solid-state spins. *Nature Photonics* **2018**, *12*, 516–527.

(8) Castelletto, S.; Boretti, A. Silicon carbide color centers for quantum applications. *Journal of Physics: Photonics* **2020**, *2*, 022001.

(9) Gottscholl, A.; Kianinia, M.; Soltamov, V.; Orlinskii, S.; Mamin, G.; Bradac, C.; Kasper, C.; Krambrock, K.; Sperlich, A.; Toth, M.; Aharonovich, I.; Dyakonov, V. Initialization and read-out of intrinsic spin defects in a van der Waals crystal at room temperature. *Nature Materials* **2020**, *19*, 540–545.

(10) Gottscholl, A.; Diez, M.; Soltamov, V.; Kasper, C.; Sperlich, A.; Kianinia, M.; Bradac, C.; Aharonovich, I.; Dyakonov, V. Room temperature coherent control of spin defects in hexagonal boron nitride. *Science Advances* **2021**, *7*, eabf3630.

(11) Gottscholl, A.; Diez, M.; Soltamov, V.; Kasper, C.; Krauße, D.; Sperlich, A.; Kianinia, M.; Bradac, C.; Aharonovich, I.; Dyakonov, V. Spin defects in hBN as promising temperature, pressure and magnetic field quantum sensors. *Nature Communications* **2021**, *12*, 4480.

(12) Liu, W. et al. Rabi oscillation of V_B^- spin in hexagonal boron nitride. **2021**, 2101.11220. arXiv. https://arxiv.org/abs/2101.11220 (accessed December 14, 2021).

(13) Gao, X.; Jiang, B.; Llacsahuanga Allcca, A. E.; Shen, K.; Sadi, M. A.; Solanki, A. B.; Ju, P.; Xu, Z.; Upadhyaya, P.; Chen, Y. P.; Bhave, S. A.; Li, T. High-Contrast Plasmonic-Enhanced Shallow Spin Defects in Hexagonal Boron Nitride for Quantum Sensing. *Nano Letters* **2021**, *21*, 7708–7714.

(14) Kianinia, M.; White, S.; Fröch, J. E.; Bradac, C.; Aharonovich, I. Generation of Spin Defects in Hexagonal Boron Nitride. *ACS Photonics* **2020**, *7*, 2147–2152.

(15) Gao, X.; Pandey, S.; Kianinia, M.; Ahn, J.; Ju, P.; Aharonovich, I.; Shivaram, N.; Li, T. Femtosecond Laser Writing of Spin Defects in Hexagonal Boron Nitride. *ACS Photonics* **2021**, *8*, 994–1000.

(16) Liu, W. et al. Temperature-Dependent Energy-Level Shifts of Spin Defects in Hexagonal Boron Nitride. *ACS Photonics* **2021**, *8*, 1889–1895.

(17) Chejanovsky, N.; Mukherjee, A.; Geng, J.; Chen, Y.-C.; Kim, Y.; Denisenko, A.; Finkler, A.; Taniguchi, T.; Watanabe, K.; Dasari, D. B. R.; Auburger, P.; Gali, A.; Smet, J. H.; Wrachtrup, J. Single-spin resonance in a van der Waals embedded paramagnetic defect. *Nature Materials* **2021**, *20*, 1079–1084.

(18) Stern, H. L.; Jarman, J.; Gu, Q.; Barker, S. E.; Mendelson, N.; Chugh, D.; Schott, S.; Tan, H. H.; Sirringhaus, H.; Aharonovich, I.; Atatüre, M. Room-temperature optically detected magnetic resonance of single defects in hexagonal boron nitride. **2021**, 2103.16494. arXiv. https://arxiv.org/abs/2103.16494 (accessed December 14, 2021).

(19) Reimers, J. R.; Shen, J.; Kianinia, M.; Bradac, C.; Aharonovich, I.; Ford, M. J.; Piecuch, P. Photoluminescence, photophysics, and photochemistry of the V_B^- defect in hexagonal boron nitride. *Phys. Rev. B* **2020**, *102*, 144105.

(20) Batalov, A.; Zierl, C.; Gaebel, T.; Neumann, P.; Chan, I.-Y.; Balasubramanian, G.; Hemmer, P. R.; Jelezko, F.; Wrachtrup, J. Temporal Coherence of Photons Emitted by Single Nitrogen-Vacancy Defect Centers in Diamond Using Optical Rabi-Oscillations. *Phys. Rev. Lett.* **2008**, *100*, 077401.

(21) Klimov, P. V.; Falk, A. L.; Christle, D. J.; Dobrovitski, V. V.; Awschalom, D. D. Quantum entanglement at ambient conditions in a macroscopic solid-state spin ensemble. *Science Advances* **2015**, *1*, e1501015.

(22) Barry, J. F.; Schloss, J. M.; Bauch, E.; Turner, M. J.; Hart, C. A.; Pham, L. M.; Walsworth, R. L. Sensitivity optimization for NV-diamond magnetometry. *Rev. Mod. Phys.* **2020**, *92*, 015004.

(23) Fuchs, G. D.; Dobrovitski, V. V.; Toyli, D. M.; Heremans, F. J.; Weis, C. D.; Schenkel, T.; Awschalom, D. D. Excited-state spin coherence of a single nitrogen–vacancy centre in diamond. *Nature Physics* **2010**, *6*, 668–672.

(24) Fuchs, G. D.; Dobrovitski, V. V.; Hanson, R.; Batra, A.; Weis, C. D.; Schenkel, T.; Awschalom, D. D. Excited-State Spectroscopy Using Single Spin Manipulation in Diamond. *Phys. Rev. Lett.* **2008**, *101*, 117601.

(25) Hanson, R.; Mendoza, F. M.; Epstein, R. J.; Awschalom, D. D. Polarization and Readout of Coupled Single Spins in Diamond. *Phys. Rev. Lett.* **2006**, *97*, 087601.

(26) Anishchik, S. V.; Ivanov, K. L. Sensitive detection of level anticrossing spectra of nitrogen vacancy centers in diamond. *Phys. Rev. B* **2017**, *96*, 115142.

(27) Mendelson, N. et al. Identifying carbon as the source of visible single-photon emission from hexagonal boron nitride. *Nature Materials* **2021**, *20*, 321–328.

(28) Epstein, R. J.; Mendoza, F. M.; Kato, Y. K.; Awschalom, D. D. Anisotropic interactions of a single spin and dark-spin spectroscopy in diamond. *Nature Physics* **2005**, *1*, 94–98.

(29) Simin, D.; Soltamov, V. A.; Poshakinskiy, A. V.; Anisimov, A. N.; Babunts, R. A.; Tolmachev, D. O.; Mokhov, E. N.; Trupke, M.; Tarasenko, S. A.; Sperlich, A.; Baranov, P. G.; Dyakonov, V.; Astakhov, G. V. All-Optical dc Nanotesla Magnetometry Using Silicon Vacancy Fine Structure in Isotopically Purified Silicon Carbide. *Phys. Rev. X* **2016**, *6*, 031014.

(30) Jacques, V.; Neumann, P.; Beck, J.; Markham, M.; Twitchen, D.; Meijer, J.; Kaiser, F.; Balasubramanian, G.; Jelezko, F.; Wrachtrup, J. Dynamic Polarization of Single Nuclear Spins by Optical Pumping of Nitrogen-Vacancy Color Centers in Diamond at Room Temperature. *Phys. Rev. Lett.* **2009**, *102*, 057403.

(31) Fischer, R.; Jarmola, A.; Kehayias, P.; Budker, D. Optical polarization of nuclear ensembles in diamond. *Phys. Rev. B* **2013**, *87*, 125207.

(32) Smeltzer, B.; McIntyre, J.; Childress, L. Robust control of individual nuclear spins in diamond. *Phys. Rev. A* **2009**, *80*, 050302.

(33) Falk, A. L.; Klimov, P. V.; Ivády, V.; Szász, K.; Christle, D. J.; Koehl, W. F.; Gali, A.; Awschalom, D. D. Optical Polarization of Nuclear Spins in Silicon Carbide. *Phys. Rev. Lett.* **2015**, *114*, 247603.

(34) Mathur, N.; Mukherjee, A.; Gao, X.; Luo, J.; McCullian, B. A.; Li, T.; Vamivakas, A. N.; Fuchs, G. D. Excited-state spin-resonance spectroscopy of V_B^- defect centers in hexagonal boron nitride. **2021**, 2111.10855. arXiv. https://arxiv.org/abs/2111.10855 (accessed December 14, 2021).

(35) Yu, P.; Sun, H.; Wang, M.; Zhang, T.; Ye, X.; Zhou, J.; Liu, H.; Wang, C.; Shi, F.; Wang, Y.; Du, J. Excited-state spectroscopy of spin defects in hexagonal boron nitride. **2021**, 2112.02912. arXiv. https://arxiv.org/abs/2112.02912 (accessed December 14, 2021). 2021.

(36) Johansson, J.; Nation, P.; Nori, F. QuTiP: An open-source Python framework for the dynamics of open quantum systems. *Computer Physics Communications* **2012**, *183*, 1760 – 1772.

(37) Johansson, J.; Nation, P.; Nori, F. QuTiP 2: A Python framework for the dynamics of open quantum systems. *Computer Physics Communications* **2013**, *184*, 1234 – 1240.